Magnetic and Electronic Properties of Zn-Doped Fe_3O_4 Hollow Nanospheres

Priyanka Saha,[1,*] Rupali Rakshit,[2] Mahebub Alam,[1] and Kalyan Mandal[1]

[1]*Department of Condensed Matter Physics and Material Science, S. N. Bose National Centre for Basic Sciences, Block JD, Sector III, Salt Lake, Kolkata 700 106*

[2]*Nanoscience & Nanotechnology Center, The Institute of Scientific and Industrial Research, Osaka University, Mihogaoka 8-1, Ibaraki, Osaka 567-0047, Japan*

(Received 6 August 2018; revised manuscript received 4 December 2018; published 22 February 2019)

Potential applications of Fe_3O_4 nanostuctures can be enhanced by preparing nanohollow spheres (NHSs) instead of nanoparticles and doping Zn to replace Fe. Detailed temperature-dependent magnetic studies of $Zn_xFe_{3-x}O_4$ ($x = 0.0$, 0.1, 0.2, 0.3, 0.4, 1.0) NHSs indicate their increase in saturation magnetization (M_S) with Zn doping, attaining a maximum at $x = 0.2$ ($M_s = 92.52$ emu/g at room temperature), due to the replacement of antiferromagnetically coupled Fe_A^{3+} ions on the A site by nonmagnetic Zn^{2+} ions and the transformation of Fe_B^{2+} to Fe_B^{3+} at the B site for maintaining the charge neutrality. The dynamic magnetic properties, studied by analyzing the real and imaginary parts of ac susceptibility, reveal the spin cluster interaction in our systems. Moreover, the investigation of dielectric properties as a function of temperature over a frequency range of 10 KHz to 100 MHz indicates the reduction in dielectric permittivity and electrical conductivity with increasing Zn content. Enhanced magnetism with a decrease in conductivity, permittivity, and dipolar interaction enables $Zn_xFe_{3-x}O_4$ NHSs to be an excellent material for high-frequency and biomedical applications.

DOI: 10.1103/PhysRevApplied.11.024059

I. INTRODUCTION

Magnetite (Fe_3O_4) in the nanoscale is one of the most important magnetic materials with a high permeability, 100% spin polarization, Verwey transition $T_V \sim 120$ K, and a very high Curie temperature, $T_c \sim 856$ K, which enable it to be a promising candidate for use in nanoscale functional spintronic devices, magnetic fluid, high-density magnetic storage, and biomedical applications [1–4]. Among all their nanostructures, nanohollow spheres (NHSs) draw maximum attention because of their low density, high compressibility to withstand changes in pressure and temperature, and large effective surface area. The lower density of hollow spheres enables them to be a better material for magnetorheological applications with higher dispersibility [5]. The hollow cavity can also be used for delivering drugs [6].

In all the applications, including biomedical, high magnetization is required. However, it deteriorates significantly when the size is reduced from bulk to nanoscale because of surface effects, where the magnetic order is highly disturbed due to the randomly oriented surface spins. Therefore, enhancement of magnetization in iron oxide nanostructures is a real challenge to material scientists. Doping Fe_3O_4 with divalent cations (Zn^{2+}, Co^{2+}, Mn^{2+}, Mg^{2+}, Ni^{2+}, etc.) is an effective method to enhance its magnetic properties [7–11]. Among these, Zn-doped Fe_3O_4 nanostructures draw great interest, in particular in clinical applications, due to the lower toxicity of Zn^{2+}. Moreover, the presence of Zn helps in forming stable complexes with various Fe_3O_4 drugs, polymers, and organic materials according to the Irving-William series [12].

In addition to a large magnetic moment, high resistivity is also required for high-frequency applications such as in microwave communication technology to reduce eddy currents, back emf, and other high-frequency-related negative effects [13,14]. With the inclusion of Zn, the conductivity of Fe_3O_4 reduces due to the reduction in spin hopping.

Magnetite and other ferrites have attracted much attention in recent years in microwave (MW) attenuation devices. MW attenuation materials must possess the properties of high absorption with minimum reflection loss. For normal incidence of a wave to an absorber layer with a metal back, reflection loss (RL) is given by [15,16]

$$\mathrm{RL}(dB) = 20 \log \left| \frac{Z-1}{Z+1} \right|, \tag{1}$$

where Z is the normalized input impedance described as

$$Z = \sqrt{\frac{\mu_r}{\epsilon_r}} \tanh \left(j \frac{2\pi t}{\lambda} \right) \sqrt{\mu_r \epsilon_r}, \tag{2}$$

*priyankasaha@bose.res.in

where μ_r and ϵ_r are the complex permeability and permittivity, λ is the wavelength of MWs in free space, and t is the thickness of the absorber.

To achieve complete absorption, Z should be equal to 1, which is possible only when $(2\pi t/\lambda)\sqrt{\mu_r\epsilon_r} = \infty$ and $\mu_r/\varepsilon_r \sim 1$. Considering the present-day requirement for miniaturization of devices, t cannot be made very large. However, μ_r can be made very high by choosing suitable materials such as ferrites. In ferrites, $\mu_r/\epsilon_r \ll 1$ as the value of ε_r is much higher than that of μ_r. Therefore, μ_r/ε_r should be tuned to unity by doping zinc, which increases μ_r due to an increase in magnetization. Hollow-structured materials can also enhance the electromagnetic absorption due to repeated reflection at the inner surface of the hollow cavity [17].

The reported magnetic properties of $Zn_xFe_{3-x}O_4$ nanomaterials prepared by different synthesis methods are contradictory. Takaobushi *et al.* [18,19] reported a continuous increase of magnetization (M_s) in $Zn_xFe_{3-x}O_4$ epitaxial thin films until $x = 0.9$. In contrast, Venkateshvaran *et al.* [20] observed the M_s of $Zn_xFe_{3-x}O_4$ epitaxial films to increase and conductivity to decrease monotonously with x from 0 to 0.5. Matsuo *et al.* [21] showed the maximum M_s for $x = 0.2$ in nanoparticles, prepared by the chemical coprecipitation method. Therefore, from the literature, we observe that Zn doping in Fe_3O_4 up to a certain percentage enhances the magnetic moment, reduces conductivity, and helps in forming stable complexes.

In this work, we prepare $Zn_xFe_{3-x}O_4$ NHSs with $0.0 \le x \le 1.0$ to investigate the relationship of the magnetic and dielectric properties with Zn doping. Maximum magnetization along with a significant reduction in conductivity is observed for $x = 0.2$.

II. EXPERIMENTAL

$Zn_xFe_{3-x}O_4$ ($x = 0.0$, 0.1, 0.2, 0.3, 0.4, 1) NHSs are synthesized using a facile template-free solvothermal method through proper variation of zinc chloride to maintain the stoichiometry for different doping percentages. In the typical synthesis of $Zn_xFe_{3-x}O_4$ NHSs, 1.35 g of $FeCl_3.6H_2O$, x g of $ZnCl_2$ ($0 \le x \le 0.291$), and 0.53 g of urea are dissolved in a 30-ml solvent mixture of 20 mL of ethylene glycol and 10 ml of ethanol, which is stirred until a clear homogeneous solution is obtained. Thereafter, 1 ml of oleylamine, which is a growth modifier as well as a surface stabilizer, is added to the solution mixture in order to restrict particle growth in the nanometer-size range. The properly mixed final solution is transferred into a 40-ml Teflon-lined stainless-steel autoclave and heated to 180 °C for 20 h followed by natural cooling to room temperature. The resulting black precipitate is thoroughly washed with absolute ethanol to remove all residual reagents and is then separated by centrifugation. The as-obtained product is dried at 60 °C for 12 h. By varying the amount of $ZnCl_2$, we are able to prepare $Zn_xFe_{3-x}O_4$ ($x = 0.0$, 0.1, 0.2, 0.4, 1) NHSs. At the elevated temperature, urea decomposes to ammonia, which is produced by hydroxyl groups. These hydroxyl groups precipitate the hydroxides of zinc and ferric ions and finally, $Zn_xFe_{3-x}O_4$ NHSs are formed.

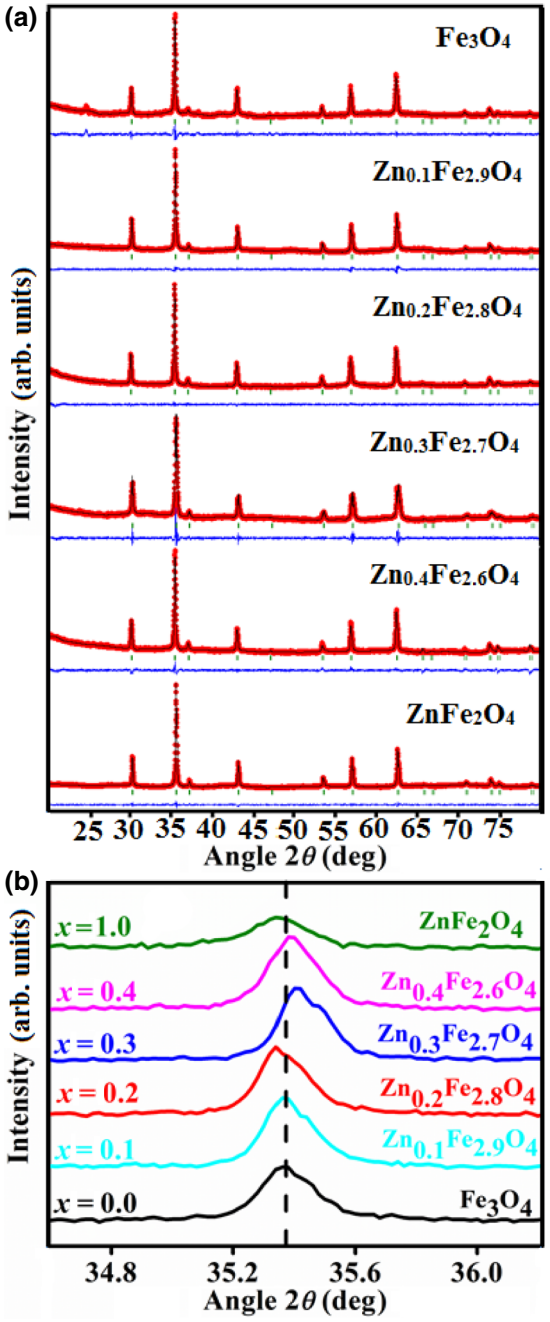

FIG. 1. (a) XRD intensity pattern of $Zn_xFe_{3-x}O_4$ ($x = 0.0$, 0.1, 0.2, 0.4, 1) with Rietveld refinement and (b) enlarged image of (311) reflection peak.

The phase and morphology of the prepared samples are characterized by a Rigaku Miniflex II desktop x-ray diffractometer using Cu K_α ($\lambda = 1.5418$ Å) radiation, FEI

TABLE I. Table for cation distribution, inversion degree (δ), and lattice parameter from Rietveld refinement.

x	$Zn_xFe_{3-x}O_4$	Lattice parameter (Å)
0.0	$Fe^{3+}[Fe^{2+}Fe^{3+}]O_4$	8.4 ± 0.0002
0.1	$\delta = 0$, $Zn^{2+}_{0.1}Fe^{3+}_{0.9}[Fe^{2+}_{0.9}Fe^{3+}_{1.1}]O_4$	8.4021 ± 0.0003
0.2	$\delta = 0.003$, $Zn^{2+}_{0.197}Fe^{3+}_{0.803}[Zn^{2+}_{0.003}Fe^{2+}_{0.8}Fe^{3+}_{1.197}]O_4$	8.4084 ± 0.0002
0.3	$\delta = 0.03$, $Zn^{2+}_{0.27}Fe^{3+}_{0.73}[Zn^{2+}_{0.03}Fe^{2+}_{0.7}Fe^{3+}_{1.27}]O_4$	8.3906 ± 0.0003
0.4	$\delta = 0.06$, $Zn^{2+}_{0.34}Fe^{3+}_{0.66}[Zn^{2+}_{0.06}Fe^{2+}_{0.6}Fe^{3+}_{1.34}]O_4$	8.4014 ± 0.0002
1.0	$\delta = 0$, $Zn^{2+}[Fe^{3+}]O_4$	8.3989 ± 0.0004

Technai G2 TF-20 TEM, and JASCO FTIR. The magnetic measurements are performed with a Lakeshore VSM and a Superconducting Quantum Interference Device (SQUID). Dielectric and ac electrical conductivity are measured using an impedance analyzer.

III. RESULTS AND DISCUSSION

A. Structure and morphology

The XRD patterns of NHSs with Rietveld refinement, shown in Fig. 1, confirm the formation of the face-centered-cubic spinel structure (JCPDS card np. 89-1397). The (311) peak [Fig. 1(b)] shifts to the lower diffraction angle up to $x = 0.2$, beyond which it moves toward the higher angle. As the tetrahedral site (A site) is larger than the octahedral site (B site), the nonmagnetic Zn^{2+} (0.74 Å) ions prefer to replace Fe^{3+} (0.64 Å) ions of the A site under a lower doping concentration, resulting in a larger lattice parameter from 8.4 Å (for $x = 0.0$) to 8.4084 Å (for $x = 0.2$) and leading to the cation distribution at the A and B sites as $(Zn^{2+}_x Fe^{3+}_{(1-x)})_A[Fe^{2+}_{(1-x)}Fe_{(1+x)}3+]_BO_4$. However, excess Zn^{2+} beyond $x = 0.2$ partly replaces Fe^{2+} ions at B sites and starts to form mixed ferrite as $[Zn^{2+}_{(x-\delta)}Fe^{3+}_{(1-x+\delta)}]_A[Zn^{2+}_{\delta}Fe^{2+}_{(1-x)}Fe^{3+}_{(1+x-\delta)}]_BO_4$, where δ is the inversion degree defined as the fraction of B sites occupied by Zn^{2+} ions. The cation distribution, δ, and lattice parameter obtained from the Rietveld refinement of the experimental XRD pattern are shown in Table I. While both the iron sites are replaced by Zn^{+2} ions, the competition between parameter b, due to the cation size effect and the Madelung constant, M, starts to play a significant role in determining the lattice constant, a, following the relation $a \propto b/M$ [22]. The substitution of more Zn^{2+} and replacement of Fe^{2+} causes a change of the repulsion potential as well as the ionic distance, resulting in the reverse trend of decreasing the lattice constant beyond $x = 0.2$. The variation of the lattice constant with Zn content is shown in Fig. 2.

The FTIR spectra of the as-prepared $Zn_xFe_{3-x}O_4$ ($x = 0$, 0.1, 0.2, 0.3, 0.4, 1) NHSs are shown in Fig. 3. Absorption bands at 576 cm^{-1} and 666 cm^{-1} are observed, which are associated with Fe-O stretching vibrations of Fe^{3+} ions in octahedral and tetrahedral sites, respectively, where the latter is absent for $x = 1.0$, confirming full doping of Zn [23]. With the substitution of zinc, a peak is observed at 430 cm^{-1} for the Zn-O stretching vibration at tetrahedral sites, confirming Zn doping.

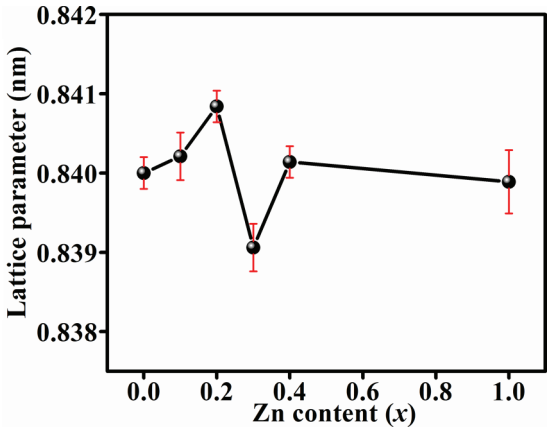

FIG. 2. Variation of lattice constant with Zn-doping concentration.

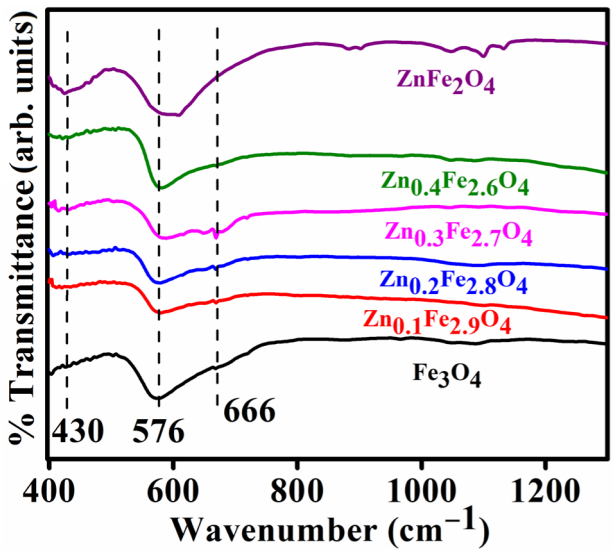

FIG. 3. FTIR spectra of the $Zn_xFe_{3-x}O_4$ NHSs.

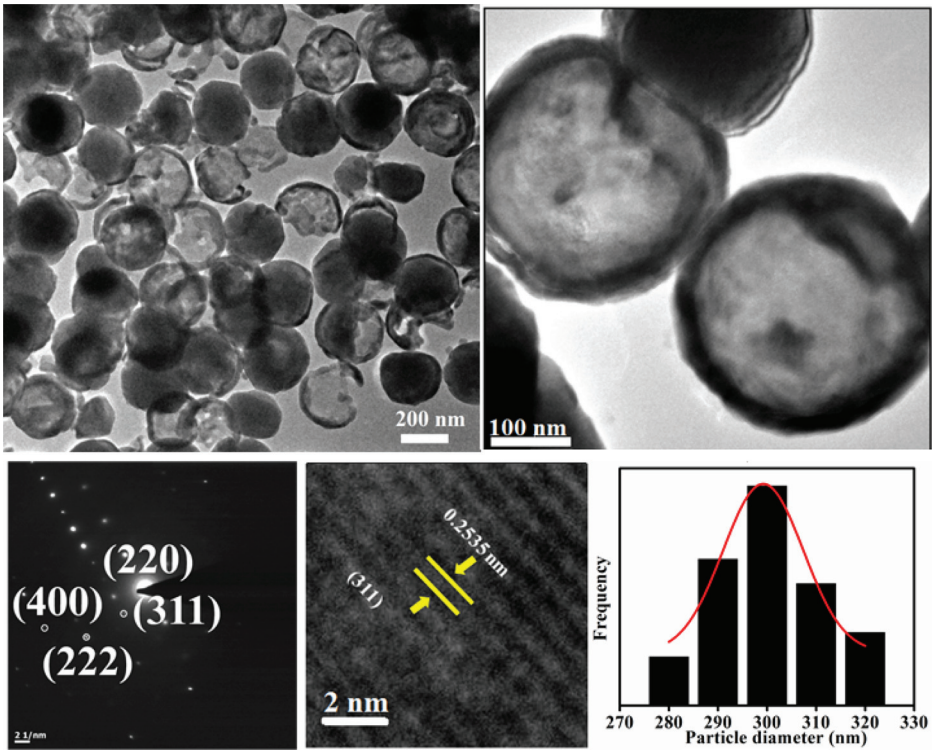

FIG. 4. TEM, High resolution TEM and SAED patterns of $Zn_{0.3}Fe_{2.7}O_4$ NHSs with size distribution.

The intensive contrast between the dark boundary line and bright center of TEM images of all the samples clearly shows the formation of NHSs with homogeneous size distribution and shell thickness. A representative TEM micrograph along with a selected area diffraction pattern (SAED), (311) plane, and size distribution curve of the sample $Zn_{0.3}Fe_{2.7}O_4$ is shown in Fig. 4. The average sizes of the NHSs calculated from the TEM images are 200–400 nm.

B. Magnetic properties

Figure 5 shows the M-H hysteresis loop of the samples at temperature $T = 300$ and 80 K. An increase in saturation magnetization (M_S) is observed upon Zn doping with maximum $M_S = 92.5$ emu-g^{-1} at 300 K and 99.5 emu-g^{-1} at 80 K for $x = 0.2$. M_s decreases on doping more Zn beyond $x = 0.2$. The magnetism in Fe_3O_4 arises due to the exchange interactions among the cations in the inverse-spinel structure, which is governed by a combination of antiferromagnetic superexchange (SE) and ferromagnetic double exchange (DE) interactions. In Fe_3O_4, the tetrahedral A site is occupied by Fe^{3+} and in the octahedral B site, there is an alternate arrangement of Fe^{3+} and Fe^{2+} ions. There are three antiferromagnetic SE interactions, J_{AA} (A-O-A), J_{BB} (B-O-B), and J_{AB} (A-O-B), between the Fe^{3+} ions on the A and B sites, mediated by the oxygen (O) ions. In addition, there is a ferromagnetic DE interaction mediated by the itinerant spin-down t_{2g} electrons hopping between the mixed-valent Fe ions on the B sites [20].

In pure Fe_3O_4, the resultant magnetization from Fe^{3+} ions is zero due to antiferromagnetic coupling and only the Fe^{2+} ions contribute to the net magnetization. With low Zn substitution, the Fe^{3+} ion on the A site is replaced by a nonmagnetic Zn^{2+} ion and it does not affect the magnetic exchange on the B site. However, for charge compensation, Fe^{2+}on the B site is converted to Fe^{3+} and nullification of the magnetic moment from Fe^{3+} is lost. As a result, M_s increases at a low substitution level ($x = 0.2$) due to the contribution from Fe^{2+} as well as Fe^{3+}. For higher substitution of Zn^{2+} ($x > 0.2$), exchange interaction J_{AB} is diluted due to nonmagnetic Zn^{2+} and saturation magnetization decreases. The variation of M_s with x is shown in the inset of Fig. 5 for both the measured temperatures.

The zero-field-cooled (ZFC) and field-cooled (FC) χ vs T measurements are shown in Fig. 6 for $Zn_xFe_{3-x}O_4$ NHSs with an applied field of 100 Oe. In the case of ZFC curves during cooling, the randomness of surface spins is frozen below a certain temperature, which is called the spin-freezing temperature (T_g), leading to a cusplike maximum around 30 K. The inset of Fig. 6 shows the variation of T_g with the Zn content (x). Higher magnetization of the FC curve compared to the corresponding ZFC curve is attributed to the surface spins, which are frozen during cooling in the direction of the external field. When nonmagnetic Zn^{2+} occupies only the A site (for $x = 0.1$, 0.2, 1.0), J_{AB} is diluted and T_g reduces. For $x = 0.3$ and $x = 0.4$, in addition to the tetrahedral site, Zn^{2+} also occupies the octahedral site, increasing the spin-orbit coupling and hence the anisotropy energy.

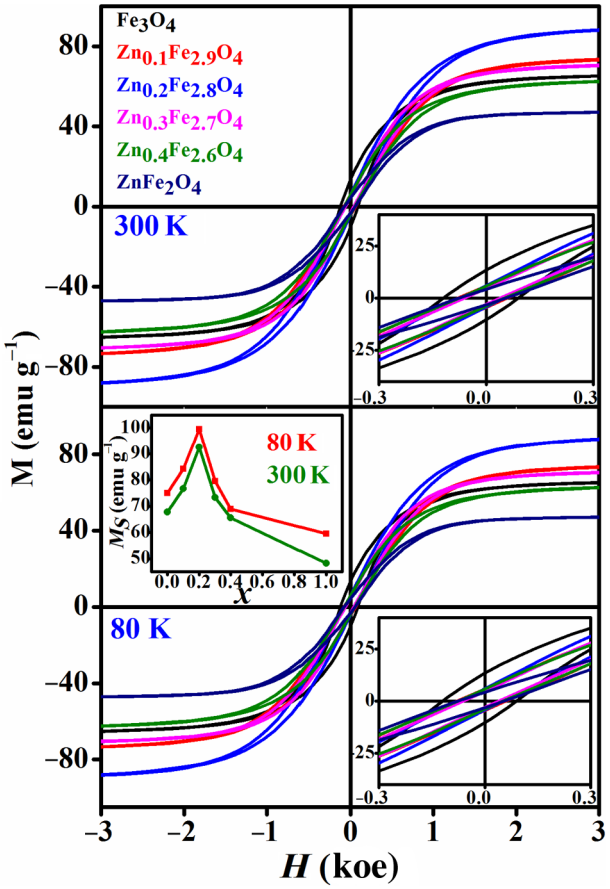

FIG. 5. Variation of magnetization (M_s) with applied magnetic field (H) at 300 and 80 K. Inset shows the variation of M_s with x at the respective measuring temperatures.

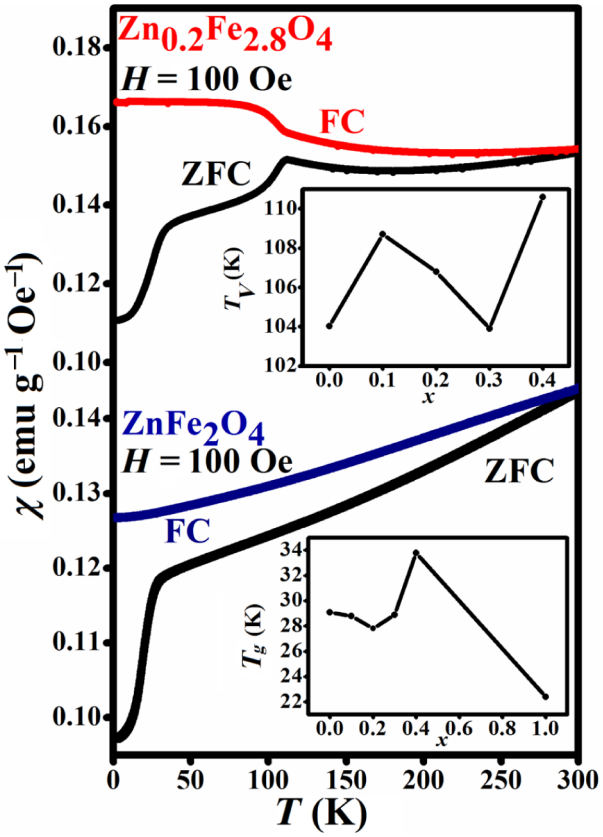

FIG. 6. ZFC-FC curves of $Zn_{0.2}Fe_{2.8}O_4$ and $ZnFe_2O_4$ (inset curves show the variation of the Verwey transition temperature and spin-freezing temperature with Zn-doping percentage x).

Another cusplike maximum observed at higher temperatures for all the samples, except for $ZnFe_2O_4$, corresponds to the Verwey transition where structural transition from cubic to monoclinic symmetry takes place. The Verwey transition temperature (T_V) is extremely sensitive to the oxygen stoichiometry or the transition metals present in the compound [24]. Since Zn^{2+} replaces Fe^{3+} at the A sites around which the vibrating oxygen ions are situated, the changes in the frequency of the phonon vibration (υ) are expected. Gupta *et al.* [24] showed the reduction in T_V with increasing phonon frequency. υ can be written as

$$\upsilon = \frac{1}{2\pi}\sqrt{\frac{k}{m_r}}, \tag{3}$$

where the reduced mass $m_r = (m_1 m_2/m_1 + m_2)$ and k is the bond strength.

Here, m_1 is the mass of Zn^{+2} / mass of Fe^{+3} and m_2 is the mass of O^{-2}. With increasing Zn^{2+} (65.408 Dalton) replacing Fe^{+3} (55.843 Dalton), m_r increases and hence υ decreases. On the other hand, the replacement of Fe^{3+} by larger Zn^{2+} changes k in the same fashion as the lattice constant, shown in Fig. 2. The resultant effect of Zn doping on T_V is shown in the inset of Fig. 6.

The real (χ') and imaginary (χ'') parts of ac susceptibility for $x = 0.0$, $x = 0.2$, and $x = 1.0$ are shown in Fig. 7 at four different frequencies, $f = 7$, 83, 253, and 503 Hz, and in the temperature range of 5 to 400 K. We observe two peaks in the susceptibility vs temperature curves. The peak at the lower temperature (T_g' for χ' and T_g'' for χ'') corresponds to the spin-freezing temperature and the second one at the higher temperature (T_V' for χ' and T_V'' for χ'') indicates the Verwey transition, which is independent of frequency [25]. With frequency, χ' does not change much except at temperatures close to and below T_g', whereas χ'' changes significantly due to the presence of magnetic dipolar interactions [26].

The frequency dependence of χ' for $T < T_g'$ and its frequency independence for $T < T_g'$ suggests the blocking process of the Fe_3O_4 NHSs [27].The variation of T_g' and T_g'' with frequency is related to the relaxation of the domain walls [28], which results in higher magnetic anisotropy as well as the spin-freezing temperature. In order to get a clearer insight into the relaxation mechanism of the NHSs, we fit the data of the relaxation time (τ) and T_g' with the

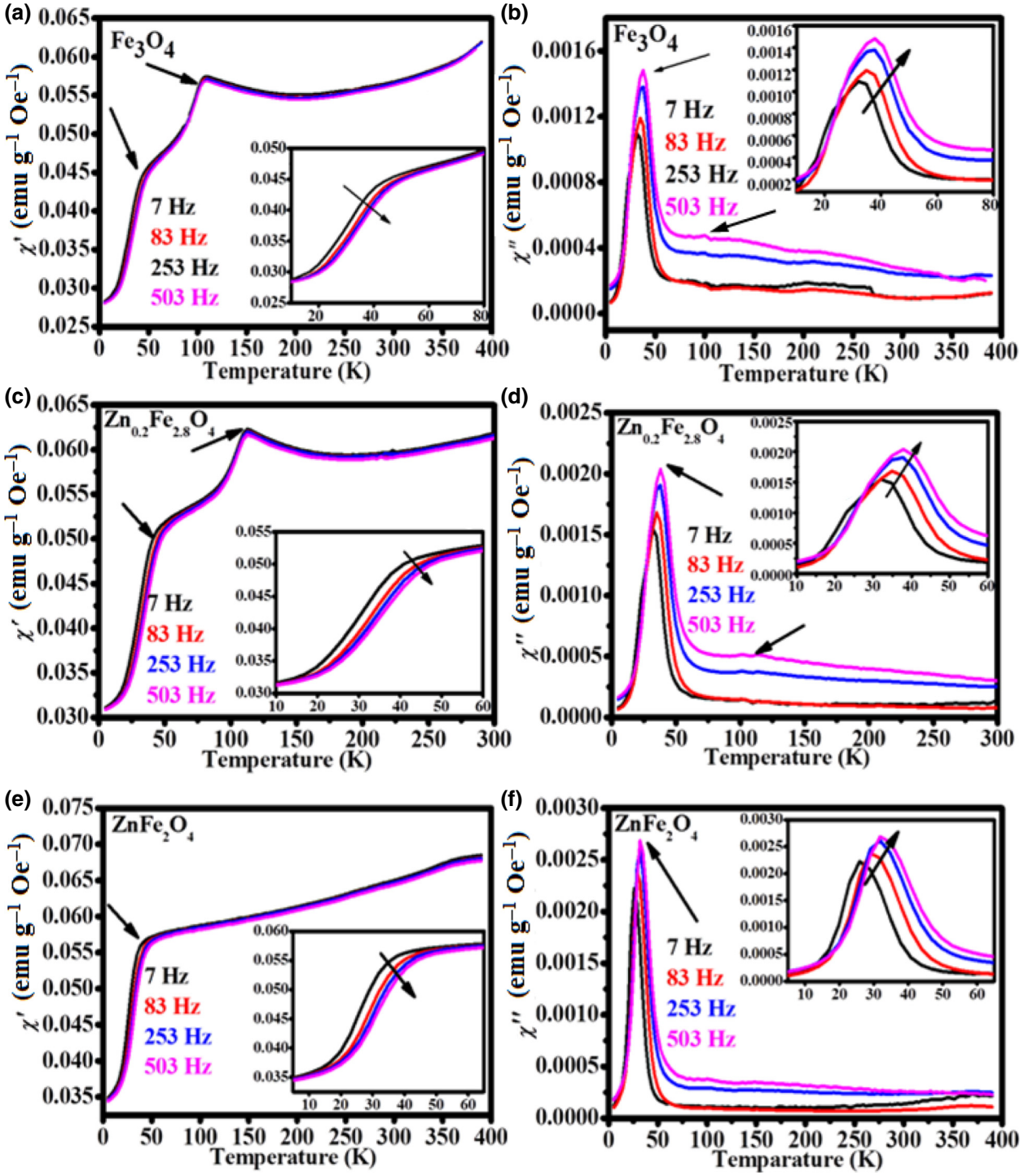

FIG. 7. Temperature-dependent susceptibility curves of (a),(b) Fe_3O_4, (c),(d) $Zn_{0.2}Fe_{2.8}O_4$, (e),(f) $ZnFe_2O_4$.

Vogel-Fulcher equation [29]:

$$\tau = \tau_0 \exp[-E_a/k_B(T_g' - T_0)], \tag{4}$$

where E_a is the anisotropy energy barrier, τ_0 is the characteristic relaxation time, k_B is the Boltzmann constant, and T_0 is the characteristic temperature, which is the measure of the interparticle interaction energy.

By fitting with Eq. (4) (Fig. 8), we find $\tau_0 = 1.14 \times 10^{-8}$ s and $T_0 = 41.0 \pm 0.2$ K for $x = 0$ for $E_a/k_B = 189$ K. This type of large τ_0 is expected for an interacting spin cluster [30]. For $x = 0.2$ and 1.0, the values of τ_0 and T_0 are 2.56×10^{-9} s and 36.0 ± 0.5 K for $E_a/k_B = 276$ K and

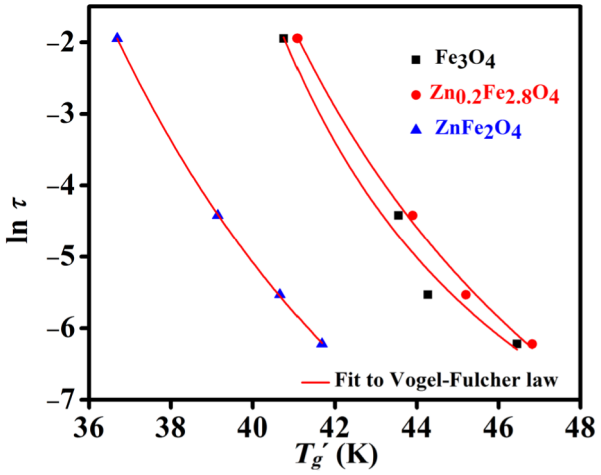

FIG. 8. Frequency dependence of T_g' fitted to the Vogel-Fulcher law.

1.53×10^{-8} s and 25 ± 0.6 K for $E_a/k_B = 219$ K, respectively. Therefore, interparticle interaction energy decreases with increasing doping, indicating a reduction in dipole interaction.

C. Dielectric properties

Figure 9 shows the variation of the real (ϵ') and imaginary (ϵ'') parts of the dielectric constant with frequency of $Zn_xFe_{3-x}O_4$ NHSs for $x = 0.0$ and 0.2 within the temperature range of 303 K $\leq$ T $\leq$ 573 K. A higher value of ϵ' is observed for the undoped Fe_3O_4 compared to the Zn-doped sample. Below 473 K, the dielectric constant is almost independent of frequency, because at lower temperatures, the thermal vibration frequency of the charge carriers does not match with the applied frequency range. With the increase in temperature as the thermal vibration is equivalent to the applied frequency, ϵ' increases, but at very high frequencies, the carriers cannot follow the applied frequency and lag behind, reducing ϵ'. The dielectric constant and dielectric loss both show high values at low frequencies and decrease with the frequency reaching a nearly saturated value indicating a frequency-independent behavior beyond 10^6 Hz. This phenomenon can be explained on the basis of Koop's theory [31]. According to this theory, the dielectric structure is said to be composed of grains and grain boundaries in which grains are conductors while grain boundaries are nonconductive. Among the various sources of polarizations, dipolar (within 10^3–10^6 Hz) and interfacial polarization (below approximately 10^3 Hz) contribute significantly. However, all polarizations cannot follow the applied frequency beyond 10^6 Hz, leading to a reduction in polarization with increasing frequency. Nyquist plots of imaginary vs real impedances ($-z''$ vs z) of the samples $x = 0$ and 0.2 are shown in Figs. 10(a) and 10(b), respectively, at different temperatures consisting of two arcs at each temperature centered at the real axis. The low- and high-frequency parts of the arcs correspond to the contributions from the grain boundary and grain, respectively. The resistance value at a particular temperature is equal to the intercept at the x axis of the corresponding semicircle.

The grain and grain boundary effect on the dielectric constant and conductivity of a material can be explained using the equivalent circuit model [32] shown in Fig. 11, consisting of two parallel RC circuits, $R_g||C_g$ (from grain) and $R_{GB}||C_{GB}$ (from grain boundary) and R_s and L_s connected in series. R_s and L_s represent the contributions from measuring leads and electrodes.

Each semicircle appearing in the Nyquist plot corresponds to the parallel RC component of the equivalent circuit. The grain resistance decreases with increasing temperature, which may be due to the change in conductivity at higher temperatures. The grain capacitance (C_g) is related to R_g via this equation:

$$\omega\tau = 2\pi f_{\max} R_g C_g = 1, \tag{5}$$

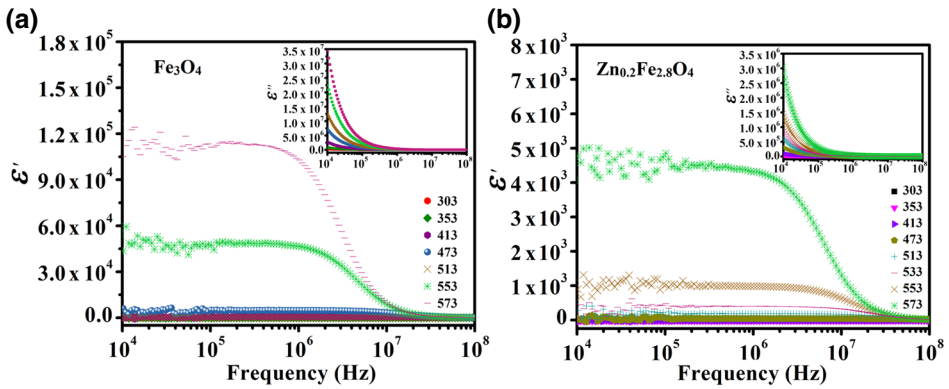

FIG. 9. Variation of dielectric constant (ϵ') with frequency at different temperatures for (a) Fe_3O_4 and (b) $Zn_{0.2}Fe_{2.8}O_4$ (inset images show the dielectric relaxation behavior over the same frequency range at different temperature values for the respective samples).

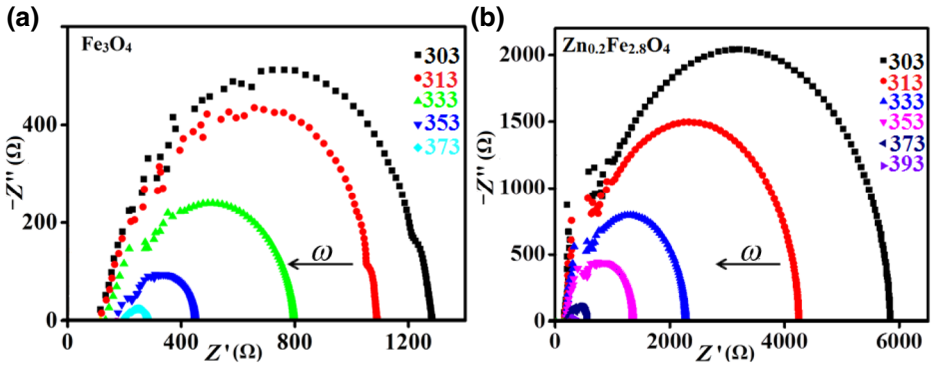

FIG. 10. Nyquist plot of (a) Fe_3O_4 and (b) $Zn_{0.2}Fe_{2.8}O_4$.

where f_{max} is the frequency maxima of the semicircle and τ is the relaxation time which follows the Arrhenius law:

$$\tau = \tau_0 \exp\left(\frac{E_r}{k_B T}\right), \tag{6}$$

where τ_0 is a prefactor, E_r is the activation energy for relaxation, T is the absolute temperature, and k_B is the Boltzmann constant. From the slope of the plot between ln τ and 1000/T (Fig. 12), the activation energy is found to be 0.01 ± 0.001 eV for Fe_3O_4 and 0.07 ± 0.009 eV for $Zn_{0.2}Fe_{2.8}O_4$. The E_r value increases with doping.

Figure 13 shows the variation of ac conductivity (σ_{ac}) with a frequency over the 10 KHz to 100 MHz range at different temperatures ranging from 303 to 573 K. Below approximately 400 K, the ac conductivity does not change significantly up to approximately 5 MHz and thereafter increases, reaching a peak value beyond which a reduction is observed. The constant conductivity at low frequency is attributed to the inability of charge carriers to cross the energy barrier; however, at higher frequencies, they gain sufficient energy to cross the barrier and increase conductivity. At very high frequencies, the carriers cannot follow the applied electric field and lag behind, resulting in a reduced σ_{ac}. Above approximately 400 K, the σ_{ac} vs frequency curve does not show any peak. Instead, a frequency-independent flat curve indicates sufficient thermal energy to cross the energy barrier.

From Fig. 13, it is clear that the ac conductivity value of $Zn_{0.2}Fe_{2.8}O_4$ NHSs is lower than that of the undoped one because of the reduction of both the spin hopping and itinerant (Fe^{2+}) charge-carrier density in the octahedral site due to doping.

The σ_{ac} of a material can be written as [33]

$$\sigma_{ac}(T) = \sigma_1(T) + \sigma_2(T), \tag{7}$$

where the first term, σ_1 (T) is the dc conductivity, which corresponds to the drift of charge carriers and the second one, σ_2 is the frequency-dependent part of the ac conductivity given by [34]

$$\sigma_2(\omega, T) = A(T)\omega^{\eta}(T), \tag{8}$$

where A has the unit of conductivity and η is dimensionless, which can be calculated from the slope of the ln (σ_{ac}) vs ln (ω) plot. Figure 14 shows the variation of η with temperature for our samples.

The nature of variation of η with temperature gives the idea of the conduction mechanism in materials depending on different models [33,35–38]: (i) conduction can be explained by quantum mechanical tunnelling (QMT) when η is independent of temperature, (ii) correlated barrier hopping (CBH) is expected when η decreases with temperature, and (iii) the increase in η with temperature

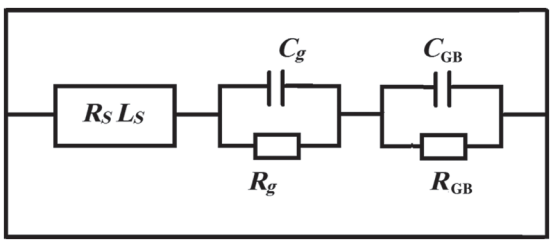

FIG. 11. Equivalent circuit, which represents the grain and grain boundary effects on the dielectric constant and conductivity.

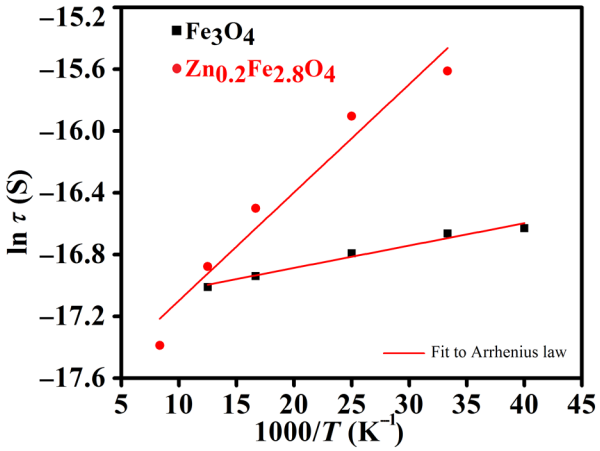

FIG. 12. Arrhenius plot of relaxation time for the samples.

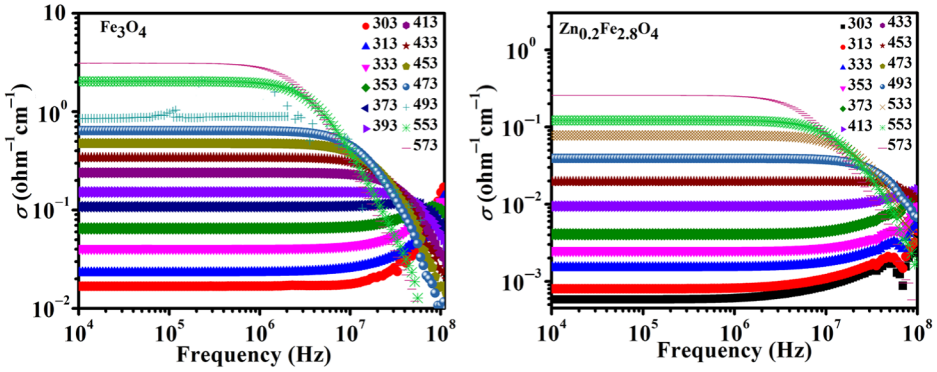

FIG. 13. Variation of ac conductivity with frequency at different temperatures for Fe_3O_4 and $Zn_{0.2}Fe_{2.8}O_4$.

can be correlated with small polaron conduction, while if η reaches a minimum followed by an increase with a further increase in temperature, then the dominant conduction mechanism is an overlapping large polaron tunnelling (OLPT). From Fig. 14, η decreases with increasing temperature, thus CBH is the conduction mechanism in undoped and Zn-doped Fe_3O_4 NHSs.

$Zn_xFe_{3-x}O_4$ nanohollow spheres with enhanced M_s (for $x = 0.2$) show reductions in both permittivity and conductivity. According to the Globus equation [39], permeability $\mu = M_s^2 D/(K)^{1/2}$, where D is the grain size and $K =$ anisotropy constant. For $x = 0.2$, μ increases due to the combined effect of the enhanced M_s and reduced anisotropy, making it a good candidate for MW attenuation devices as per Eqs. (1) and (2) as discussed earlier. Higher μ_r and nanohollow structures help in developing thin and lightweight MW absorbers.

The reflection coefficient (R) at the air-material interface for normal incidence of the electromagnetic wave, follows the equation:

$$R = \left| \frac{\sqrt{(\mu_r/\epsilon_r)} - 1}{\sqrt{(\mu_r/\epsilon_r)} + 1} \right| . \tag{9}$$

Therefore, $R \sim 1$ when the value of ε_r is much higher than that of μ_r. $Zn_{0.2}Fe_{2.8}O_4$ NHS with increased μ_r and two orders of magnitude less ε_r (compared to that of $x = 0$) can be an excellent material for MW attenuation devices.

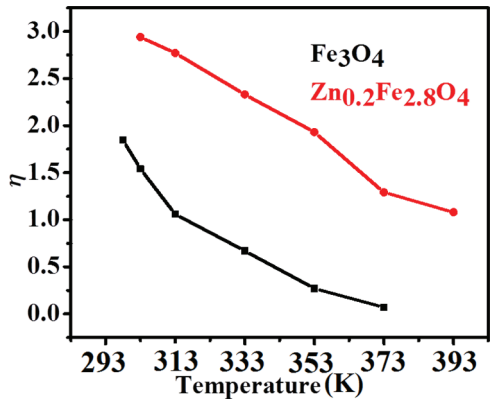

FIG. 14. Variation of η with temperature.

IV. CONCLUSION

In conclusion, $Zn_xFe_{3-x}O_4$ nanohollow spheres are successfully prepared with a higher value of saturation magnetization reaching a maximum at $x = 0.2$. We find an increase in resistivity with Zn doping due to a reduction in spin hopping, which is effective in reducing eddy currents, back emf, and other high-frequency-related negative effects. $Zn_{0.2}Fe_{2.8}O_4$ NHSs can be excellent materials for thin and lightweight MW attenuation devices and other high-frequency communication technologies. The presence of biocompatible Zn also helps in forming stable complexes with various drugs, polymers, and organic materials, making it a promising material for biomedical applications.

ACKNOWLEDGMENTS

P. Saha is grateful to the Department of Science and Technology (INSPIRE), Government of India, for financial support. Funding from SNBNCBS is also gratefully acknowledged.

[1] S. Laurent, D. Forge, M. Port, A. Roch, C. Robic, L. Vander Elst, and R. N. Muller, Magnetic iron oxide nanoparticles: Synthesis, stabilization, vectorization, physicochemical characterizations, and biological applications, Chem. Rev. **108**, 2064 (2008).

[2] J. P. Hong, S. B. Lee, Y. W. Jung, J. H. Lee, K. S. Yoon, K. W. Kim, C. O. Kim, and C. H. Lee, Room temperature formation of half-metallic Fe_3O_4 thin films for the application of spintronic devices, Appl. Phys. Lett. **83**, 1590 (2003).

[3] H. Liu, E. Y. Jiang, H. L. Bai, R. K. Zheng, H. L. Wei, and X. X. Zhang, Large room temperature spin-dependent tunneling magnetoresistance in polycrystalline Fe_3O_4 films, Appl. Phys. Lett. **83**, 3531 (2003).

[4] X. Wang, R. Zhang, C. Wu, Y. Dai, M. Song, S. Gutmann, F. Gao, G. Lv, J. Li, X. Li, Z. Guan, D. Fu, and B. Chen, The application of Fe_3O_4 nanoparticles in cancer research:

A new strategy to inhibit drug resistance, J. Biomed. Mater. Res. **80A**, 852 (2007).

[5] X. Ruan, L. Pei, S. Xuan, Q. Yan, and X. Gong, The rheological responds of the superparamagnetic fluid based on Fe_3O_4 hollow nanospheres, J. Magn. Magn. Mater. **429**, 1 (2017).

[6] D. H. M. Buchold and C. Feldmann, Nanoscale γ-AlO(OH) hollow spheres: Synthesis and container-type functionality, Nano Lett. **7**, 3489 (2007).

[7] C. Yao, Q. Zeng, G. F. Goya, T. Torres, J. Liu, H. Wu, M. Ge, Y. Zeng, Y. Wang, and J. Z. Jiang, $ZnFe_2O_4$ nanocrystals: Synthesis and magnetic properties, J. Phys. Chem. C **111**, 12274 (2007).

[8] G. V. M. Jacintho, A. G. Brolo, P. Corio, P. A. Z. Suarez, and J. C. Rubim, Structural investigation of MFe_2O_4 (M = Fe, Co) magnetic fluids, J. Phys. Chem. C **113**, 7684 (2009).

[9] Q. He, H. Z. Wang, G. H. Wen, Y. Sun, and B. Yao, Formation and properties of $Ba_xFe_{3-x}O_4$ with spinel structure by mechanochemical reaction of α-Fe_2O_3 and $BaCO_3$, J. Alloys Compd. **486**, 246 (2009).

[10] L. Li, G. Li, R. L. Smith, and H. Inomata, Microstructural evolution and magnetic properties of $NiFe_2O_4$ nanocrystals dispersed in amorphous silica, Chem. Mater. **12**, 3705 (2000).

[11] M. Mozaffari, S. Manouchehri, M. H. Yousefi, and J. Amighian, The effect of solution temperature on crystallite size and magnetic properties of Zn substituted Co ferrite nanoparticles, J. Magn. Magn. Mater. **322**, 383 (2010).

[12] H. Irving and R. J. P. Williams, 637. The stability of transition-metal complexes, J. Chem. Soc. **0**, 3192 (1953).

[13] M. Maaß, A. Griessner, V. Steixner, and C. Zierhofer, Reduction of eddy current losses in inductive transmission systems with ferrite sheets, BioMed. Eng. OnLine **16**, 3 (2017).

[14] H. A. Sabbagh, A model of eddy-current probes with ferrite cores, in *Review of Progress in Quantitative Nondestructive Evaluation*, edited by D. O. Thompson and D. E. Chimenti (Springer, Boston, MA, 1983), pp. 1173–1185.

[15] S. S. Kim, S. B. Jo, K. I. Gueon, K. K. Choi, J. M. Kim, and K. S. Churn, Complex permeability and permittivity and microwave absorption of ferrite-rubber composite at X-band frequencies, IEEE Trans. Magn. **27**, 5462 (1991).

[16] P. Singh, V. K. Babbar, A. Razdan, R. K. Puri, and T. C. Goel, Complex permittivity, permeability, and X-band microwave absorption of CaCoTi ferrite composites, J. Appl. Phys. **87**, 4362 (2000).

[17] M. Han, X. Yin, L. Kong, M. Li, W. Duan, L. Zhang, and L. Cheng, Graphene-wrapped ZnO hollow spheres with enhanced electromagnetic wave absorption properties, J. Mater. Chem. A **2**, 16403 (2014).

[18] J. Takaobushi, M. Ishikawa, S. Ueda, E. Ikenaga, J. J. Kim, M. Kobata, Y. Takeda, Y. Saitoh, M. Yabashi, Y. Nishino, D. Miwa, K. Tamasaku, T. Ishikawa, I. Satoh, H. Tanaka, K. Kobayashi, and T. Kawai, Electronic structures of $Fe_{3-x}M_xO4$(M = Mn, Zn) spinel oxide thin films investigated by x-ray photoemission spectroscopy and x-ray magnetic circular dichroism, Phys. Rev. B **76**, 205108 (2007).

[19] J. Takaobushi, H. Tanaka, T. Kawai, S. Ueda, J. Kim, M. Kobata, E. Ikenaga, M. Yabashi, K. Kobayashi, Y. Nishino, D. Miwa, K. Tamasaku, and T. Ishikawa, $Fe_{3-x}Zn_xO4$ thin film as tunable high Curie temperature ferromagnetic semiconductor, Appl. Phys. Lett. **89**, 242507 (2006).

[20] D. Venkateshvaran, M. Althammer, A. Nielsen, S. Geprägs, M. S. Ramachandra Rao, S. T. B. Goennenwein, M. Opel, and R. Gross, Epitaxial $Zn_xFe_{3-x}O_4$ thin films: A spintronic material with tunable electrical and magnetic properties, Phys. Rev. B **79**, 134405 (2009).

[21] J. liu, Y. Bin, and M. Matsuo, Magnetic behavior of Zn-doped Fe_3O_4 nanoparticles estimated in terms of crystal domain size, J. Phys. Chem. C **116**, 134 (2012).

[22] A. R. Das, V. S. Ananthan, and D. C. Khan, Lattice parameter variation and magnetization studies on titanium, zirconium, and tin-substituted nickel-zinc ferrites, J. Appl. Phys. **57**, 4189 (1985).

[23] Z. R. Marand, M. H. R. Farimani, and N. Shahtahmasebi, Study of magnetic and structural and optical properties of Zn doped Fe_3O_4 nanoparticles synthesized by co-precipitation method for biomedical application, Nanomed. J. **1**, 238 (2014).

[24] R. Gupta, A. K. Sood, P. Metcalf, and J. M. Honig, Raman study of stoichiometric and Zn-doped Fe_3O_4, Phys. Rev. B **65**, 104430 (2002).

[25] D. A. Clark and P. W. Schmidt, Theoretical analysis of thermomagnetic properties, low-temperature hysteresis and domain structure of titanaomagnetites, Phys. Earth Planet. Inter. **30**, 300 (1982).

[26] G. T. Landi, F. R. Arantes, D. R. Cornejo, A. F. Bakuzis, I. Andreu, and E. Natividad, AC susceptibility as a tool to probe the dipolar interaction in magnetic Nanoparticles, J. Magn. Magn. Mater. **421**, 138 (2017).

[27] J. L. Dorman, D. Fiorani, and E. Tronc, Magnetic relaxation in fine-particle systems, Adv. Chem. Phys. **98**, 283 (1997).

[28] Z. Šimša, F. Zounová, and S. Krupička, Initial permeability of single crystal magnetite and Mn-ferrite, Czech. J. Phys. B **35**, 1271 (1985).

[29] J. L. Tholence, On the frequency dependence of the transition temperature in spin glasses, Solid State Commun. **35**, 113 (1980).

[30] B. Idzikowski, U. K. Rößler, D. Eckert, K. Nenkov, K. Dörr, and K. H. Müller, Spin-glass–like ordering in giant magnetoresistive CuCo, Euro phys. Lett. **45**, 714 (1999).

[31] B. D. Cullity, *Introduction to Magnetic Materials* (Wesley Reading, New York, 1972), p. 355.

[32] R. Das, T. Sarkar, and K. Mandal, Multiferroic properties of Ba^{2+} and Gd^{3+} co-doped bismuth ferrite: Magnetic, ferroelectric and impedance spectroscopic analysis, J. Phys. D: Appl. Phys. **45**, 455002 (2012).

[33] E. V. Gopalan, K. A. Malini, S. Saravanan, D. S. Kumar, Y. Yoshida, and M. R. Anantharaman, Evidence for polaron conduction in nanostructured manganese ferrite, J. Phys. D: Appl. Phys. **41**, 185005 (2008).

[34] A. K. Jonscher, The "universal" dielectric response, Nature **267**, 673 (1977).

[35] P. Pandit, S. Satapathy, and P. K. Gupta, Effect of La substitution on conductivity and dielectric properties of $Bi_{1-x}La_xFeO_3$ ceramics: An impedance spectroscopy analysis, Phys. B **406**, 2669 (2011).

[36] T. M. Meaz, S. M. Attia, A. M, and Abo El Ata, Effect of tetravalent titanium ions substitution on the dielectric properties of Co–Zn ferrites, J. Magn. Magn. Mater. **257**, 296 (2003).

[37] A. Ghosh, ac conduction in iron bismuthate glassy semiconductors, Phys. Rev. B **42**, 1388 (1990).

[38] M. K. Fayek, M. F. Mostafa, F. Sayedahmed, S. S. Ata-Allah, and M. Kaiser, On the electrical behavior of nickel ferrite-gallates, J. Magn. Magn. Mater. **210**, 189 (2000).

[39] A. Globus and P. Duplex, Separation of susceptibility mechanisms for ferrites of low anisotropy, IEEE Trans. Magn. **2**, 441 (1966).